# Real-time, in situ viscosity mapping of active lava

Martin A. Harris, Oryaëlle Chevrel, Jason Travis Parsons, Thierry Latchimy, Thorvaldur Thordarson, Ármann Höskuldsson, William Moreland, Méline Payet–Clerc, Stephan Kolzenburg

https://doi.org/10.1130/G52558.1
Manuscript accepted 5 November 2024 - Geology

# Real-time, *in-situ* viscosity mapping of active lava

M.A. Harris[1*], M.O. Chevrel[1,2,3,4] , J.T. Parsons[1], T. Latchimy[2] , T. Thordarson[5], A. Höskuldsson[6], W.M. Moreland[5], M. Payet—Clerc[3,5], S. Kolzenburg[1]

[1] Department of Geology, State University of New York at Buffalo, 126 Cooke Hall Buffalo, New York 14260-4130, USA
[2] Université Clermont Auvergne, CNRS, IRD, OPGC, Laboratoire Magmas et Volcans, F-63000 Clermont-Ferrand, France
[3] Université Paris Cité, Institut de Physique du Globe de Paris, CNRS, 75005 Paris, France
[4] Observatoire Volcanologique du Piton de la Fournaise, Institut de Physique du Globe de Paris, 97418 La Plaine des Cafres, France
[5] Faculty of Earth Sciences, University of Iceland, Sturlugata 7, IS-102 Reykjavík, Iceland
[6] Nordic Volcanological Centre, Institute of Earth Sciences, University of Iceland, Sturlugata 7, IS-102 Reykjavík, Iceland

## ABSTRACT

Viscosity is a fundamental physical property that controls lava flow dynamics, runout distance, and velocity, which are critical factors in assessing and mitigating risks associated with effusive eruptions. Natural lava viscosity is driven by a dynamic interplay among melt, crystals, and bubbles in response to the emplacement conditions. These conditions are challenging to replicate in laboratory experiments, yet this remains the most common method for quantifying lava rheology. Few in situ viscosity measurements exist, but none of those constrains the spatial evolution of viscosity along an entire active lava flow field. Here, we present the first real-time, in situ viscosity map of active lava as measured in the field at Litli-Hrútur, Iceland. We precisely measured a lava viscosity increase of over two orders of magnitude, associated with a temperature decrease, crystallinity increase, and vesicularity decrease from near-vent to distal locations, crossing the pāhoehoe–‘a‘ā transition. Our data expand the limited database of three-phase lava viscosity, which is crucial for improvements and validation of the current numerical, experimental, and petrological approaches used to estimate lava viscosity. Further, this study showcases that field viscometry provides a rapid, accurate, and precise assessment of lava viscosity that can be implemented in eruptive response modeling of lava transport.

## 1. INTRODUCTION

Eruptive style, flow velocity, morphology, and runout distance are controlled by viscosity. Viscosity parameterizations have largely been derived from analog materials and re-melted rocks in the laboratory (Mader

* martin.a.harris95@gmail.com

et al., 2013, Kolzenburg et al., 2022). Laboratory experiments allow for precise control of temperature, shear rate, and oxygen fugacity, but they struggle to reproduce the three-phase nature (melt+crystals+bubbles) of lava, as they usually lack a gas phase. Viscosity determinations of active lava have proven effective at capturing bulk properties but the methods rely on observations of channelized lavas and quantification of the flow rate (*e.g.,* Moore, 1987; Fink and Zimbelman, 1990; Lev and James, 2014). Note that any measurement of three-phase suspensions represents a single point of apparent viscosity along the materials flow curve, we use the term viscosity in this manuscript for brevity.

Viscosity data is used in lava flow models to aid the forecasting of flow paths and runouts (Harris and Rowland, 2001; Costa and Macedonio, 2005; Cappello et al., 2016; Hyman et al., 2022). Rapid viscosity determinations have been sought after for decades and current approaches like channel velocity estimates and petrographic modeling have been done for recent eruptions (*e.g.,* Kilauea; Dietterich et al., 2021; Cumbre Vieja; Pankhurst et al., 2022; Piton de la Fournaise; Chevrel et al., 2022). However, if channel geometry, topography, and effusion rate assumptions are used for viscosity determinations, their uncertainties propagate to the predicted flow paths. Additionally, petrographic methods require at least several days to process lava texture and chemistry needed for the viscosity estimate.

Alternatively, *in-situ* viscosity measurements of lava provide a direct value and yield detailed information on the dynamic, three-phase lava viscosity (Chevrel et al., 2018a). To date, *in-situ* measurements have been decoupled from laboratory studies and scarcely implemented at isolated locations (Chevrel et al., 2019). This is largely due to a lack of portable and accurate measurement devices. Recent advances have provided two new portable field viscometers: a motor-driven rotational viscometer (RV) by Chevrel et al., (2023) for low viscosities ($10^1$-$10^3$ Pa·s), and a lava penetrometer (LP) by Harris et al., (2024) for medium to high viscosities ($10^3$-$10^5$ Pa·s).

Here, using these devices, we present the first set of *in-situ* viscosity measurements that cover an entire active lava flow. Measurements were performed at the Litli-Hrútur eruption on the Reykjanes Peninsula, Iceland (Fig. 1). The mean output rate was 4±2 $m^3/s$ with an eruptive volume of 12 $Mm^3$ DRE (Thordarson et al., 2023). The composition of the erupted lava is tholeiitic basalt (see Supplement S1) with porphyritic plagioclase (15-25%) and minor olivine (2-5%) phenocrysts. Our measurements provide unprecedented viscosity data associated with temperature and vesicularity and increasing crystallinity along the flow, including a constraint over the pāhoehoe - 'a'ā transition.

This study showcases the potential for *in-situ* measurements to recover detailed three-phase lava rheology at significantly faster timescales than currently used methods. Such data can be used to improve or validate the understanding of multiphase lava rheology. Rapid and precise field-viscometry, as done here for the first time for an entire flow field, can also promote enhanced real-time models of lava flow propagation used in civil protection efforts.

## 2. METHODS

We conducted viscosity measurements at six locations (Fig. 1C) from July 17-26 starting 7 days after the eruption onset (S2). The lava flowed on a flat-lying valley, in a channel that transitioned from pāhoehoe to 'a'ā after ~2 km. The channel was inaccessible but repeated partial collapse of the vent led to channel overflows and breakouts that made lava accessible for measurements. The

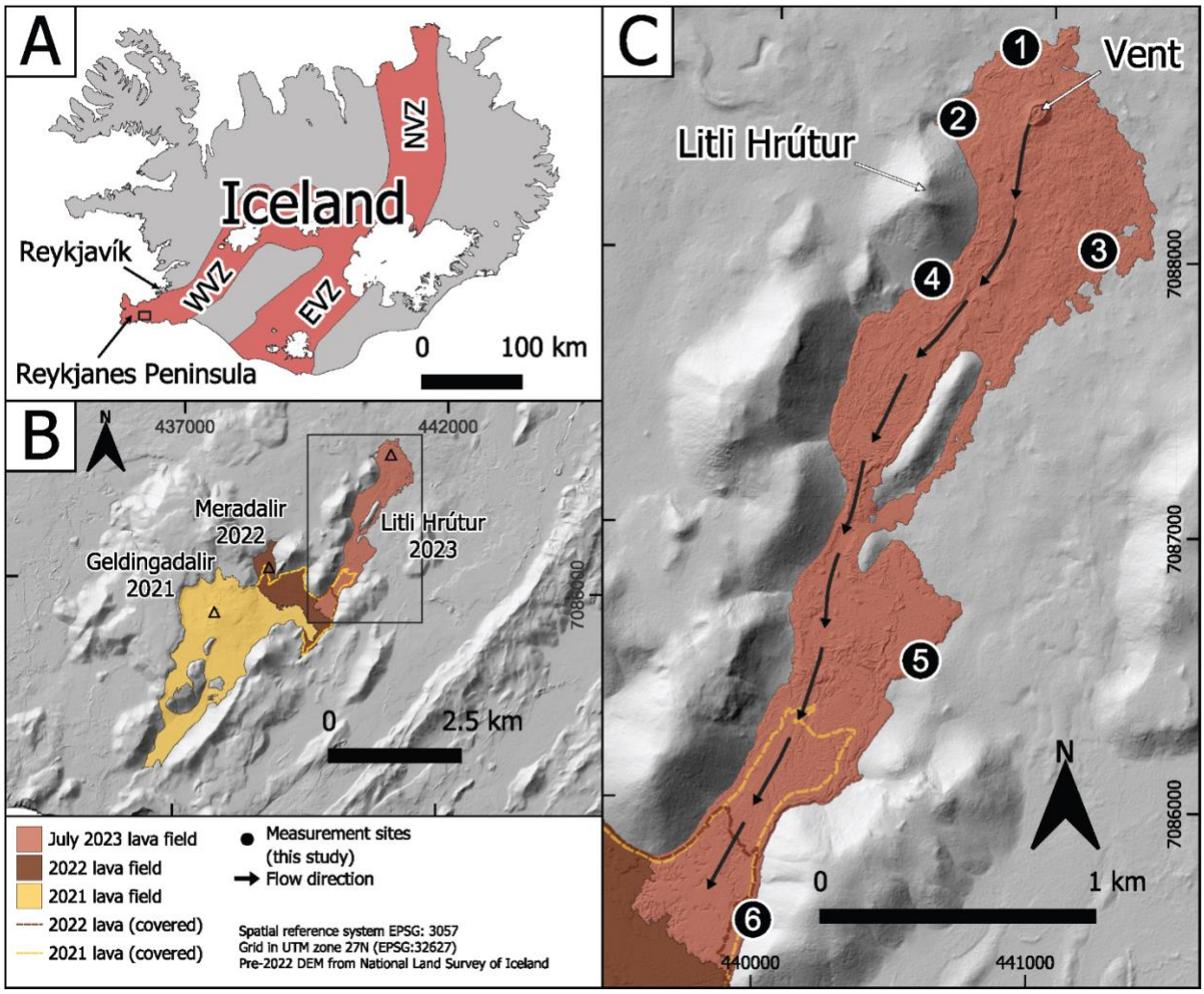


*Figure 1 Location of the measurement sites on the lava flow field of 2023 Litli-Hrútur, Iceland. A) Regional setting of the eruption site within the southwest Reykjanes Peninsula. The black rectangle denotes the submap B location. Rift zones (red) and ice caps (white) are shown. B) Map showing the extent of the 2021, 2022, and 2023 lava flow fields in the area. Triangles denote approximate vent locations. The black rectangle denotes the submap C location. C) Map showing the extent of the lava flow field with the six measurement site locations.*

sample collected 250 m from the vent, at Site 1, is consistent with the textural and chemical properties of vent spatters (Krmíček et al., 2023), and we document the three-phase textural and thermal evolution of all remaining sites down to the flow front at 3200 m from the vent (Table 1).

As a result, we consider the textural and thermal properties of the measured lavas to be representative of lava during flow in the entire system.

RV measurements were performed at Sites 1 and 3, in breakout pāhoehoe lobes. They record the torque of a rotating shear vane immersed in the lava for one to three minutes (Fig. 2A). LP measurements were performed at Sites 2, 3, 4, 5, and 6, in pāhoehoe lobes and windows of accessible 'a'ā lava at the flow front. They record the force required to push a hemispherical indenter into the lava for ~20 cm, for ~2-15 seconds (Fig. 2C). Both devices are open-source; specifications and calibration to


*Figure 2: Field photos of the six sites where viscosity and temperature measurements as well as sampling were performed. A) Site 1, using the rotational viscometer within sheet pāhoehoe lavas. B) Site 2, sampling of spiny pāhoehoe lavas. C) Site 3, using the lava penetrometer within spiny pāhoehoe lavas. D) Site 4, using the lava penetrometer within transitional spiny pāhoehoe lavas. E) Site 5, sampling lava on a rubbly 'a'ā flow front. F) Site 6, performing temperature measurement on the 'a'ā lava flow front.*

directly recover viscosity are presented in Chevrel et al., (2023), Harris et al., (2024), and in S3.

Lava temperatures were measured at each site using K-type thermocouples immersed at ~10-20 cm depth for 2-3 minutes (Fig. 2F), and measurements with a stable reading over ~50 seconds were deemed valid. Samples were collected at each site (Figs. 2B and 2E) and quenched in water to suppress further crystallization and maintain the textures of the lava while flowing. Representative material was used to quantify crystals and vesicles (area %) (S4). We used Thermobar (Wieser et al., 2022) to calculate pressure and water-independent glass temperatures from electron microprobe-derived glass MgO analyses for each site ( Fig. 3; S1 and S2).

## 3. RESULTS

The lava morphology transitioned over a distance of 3200 m from sheet and slabby pāhoehoe (sites 1 to 3) near the vent to transitional spiney pāhoehoe (site 4), rubbly 'a'ā (site 5), and blocky 'a'ā (site 6) in the distal sectors of the flow field (Fig. 2; Table 1). We recorded *in-situ* temperatures for 5 of the 6 sites, recovering a decrease of lava temperature from 1165-1148 °C, over a distance of 3.2 km, equating to a cooling rate of 4.9°C/km (Fig. 3A). The calculated glass temperatures systematically underestimated the lava temperatures by ~5℃ compared with *in-situ* measurements, although the cooling rate remains similar (4.1°C/km). We measured an increase in viscosity, from 322 Pa·s near the vent to 37770 Pa·s at the flow front (Fig. 3C and D; Tables 1 and S2). Lava groundmass crystallinity along the path increases from ~25% to ~50% and vesicularity decreases from 32% to 2% (Fig. 3B; Tables 1 and S2).

At site 3 where both field rheometers were used, we recovered *in-situ* viscosities

| Site # | UTM E | UTM N | Measurement type | Viscosity (Pa s) | 2σ | Temperature (°C) | Crystal % | 2σ | Bubble% | 2σ | Distance fro vent (m) |
|---|---|---|---|---|---|---|---|---|---|---|---|
| 1 | 440846 | 7088729 | Rotational$^{80}$ | 322 | 77 | 1165 | 25 | 1 | 32 | 5 | 250 |
| 2 | 440626 | 7088462 | Penetrometer | 399 | 48 | 1164 | 30 | 2 | 15 | 5 | 370 |
| 3$^{1}$ | 441154 | 7087999 | Rotational$^{80}$ | 2521 | 85 | 1161 | 27 | 4 | 20 | 11 | 650 |
| 3$^{1}$ | 441154 | 7087999 | Rotational$^{30}$ | 3270 | 1548 | 1161 | 27 | 4 | 20 | 11 | 650 |
| 3$^{1}$ | 441154 | 7087999 | Penetrometer | 643 | 155 | 1161 | 27 | 4 | 20 | 11 | 650 |
| 3$^{2}$ | 441154 | 7087999 | Rotational$^{30}$ | 3571 | 456 | 1162 | - | - | 17 | 6 | 650 |
| 3$^{2}$ | 440551 | 7087877 | Rotational$^{60}$ | 2008 | 614 | 1162 | - | - | 17 | 6 | 650 |
| 4 | 440551 | 7087877 | Penetrometer | 1302 | 304 | 1163 | 33 | 3 | 12 | 6 | 900 |
| 5 | 440625 | 7086421 | Penetrometer | 5311 | 913 | 1155* | 47 | 2 | 12 | 6 | 2400 |
| 6 | 439971 | 7085528 | Penetrometer | 19439 | 1355 | 1150 | 51 | 5 | 2 | 1 | 3200 |
| 6 | 439971 | 7085528 | Penetrometer | 37679 | 4563 | 1148 | 51 | 5 | 2 | 1 | 3200 |
| 6 | 439971 | 7085528 | Penetrometer | 13963 | 1480 | 1152 | 51 | 5 | 2 | 1 | 3200 |

*Table 1 Summary of viscosity and temperature measurements and sample textures for each site.*

Rotational Shear Vane Sizes: $^{80}$=80x25 mm; $^{60}$=60x20 mm; $^{30}$=30x15 mm
3$^{1}$ = Measurements conducted at Site 3 on 25 July 2023, 3$^{2}$ = Measurements conducted at Site 3 on 26 July 2023
*Obtained from corrected glass temperature

that span 643 Pa·s (LP) to 2000-3500 Pa·s (RV). This variation is explained by thermal gradients within the lavas. The LP viscosities are measured at depths of ~10-15 cm within the lava (Harris et al., 2024) where the independent thermocouple measurements were recorded, whereas the depths for RV measurements are closer to the surface within ~5-10 cm. Thus, the LP data represent the hotter interior, and the RV data represent cooler crust, potentially entering the viscoelastic regime (Pinkerton and Sparks, 1978; James et al., 2004). *In-situ* techniques can therefore quantify the change in viscosity of the viscous horizon along the outer boundary of the lava (Belousov and Belousova, 2018), which excerpts the most significant control on the flow at active lava fronts and margins.

## 4. DISCUSSION

### 4.1 Temperature, Viscosity, and Textural Evolution of Lavas

Since the composition of the Litli-Hrútur lavas did not change within the flow field (S1), any change in viscosity along the ~3km (Fig.3) flow is the result of thermal and textural changes within the lava. Prior work on suspension rheology has shown that increasing the particle fraction of a suspension towards the maximum packing fraction (~50-70%) causes an exponential increase in effective viscosity due to particle jamming, followed by flattening of effective viscosity at very high particle fractions (Costa et al., 2009). Additionally, the bubble fraction within a suspension has been shown to decrease the effective viscosity when the capillary number (Ca) > 1, where bubbles deform, and increase effective viscosity when Ca < 1 when bubbles act as rigid solids (Mader et al., 2013).

The pāhoehoe - 'a'ā transition is driven by cooling and crystallization, increasing lava viscosity (Cashman et al., 1999; Robert et al., 2014; Di Fiore et al.,

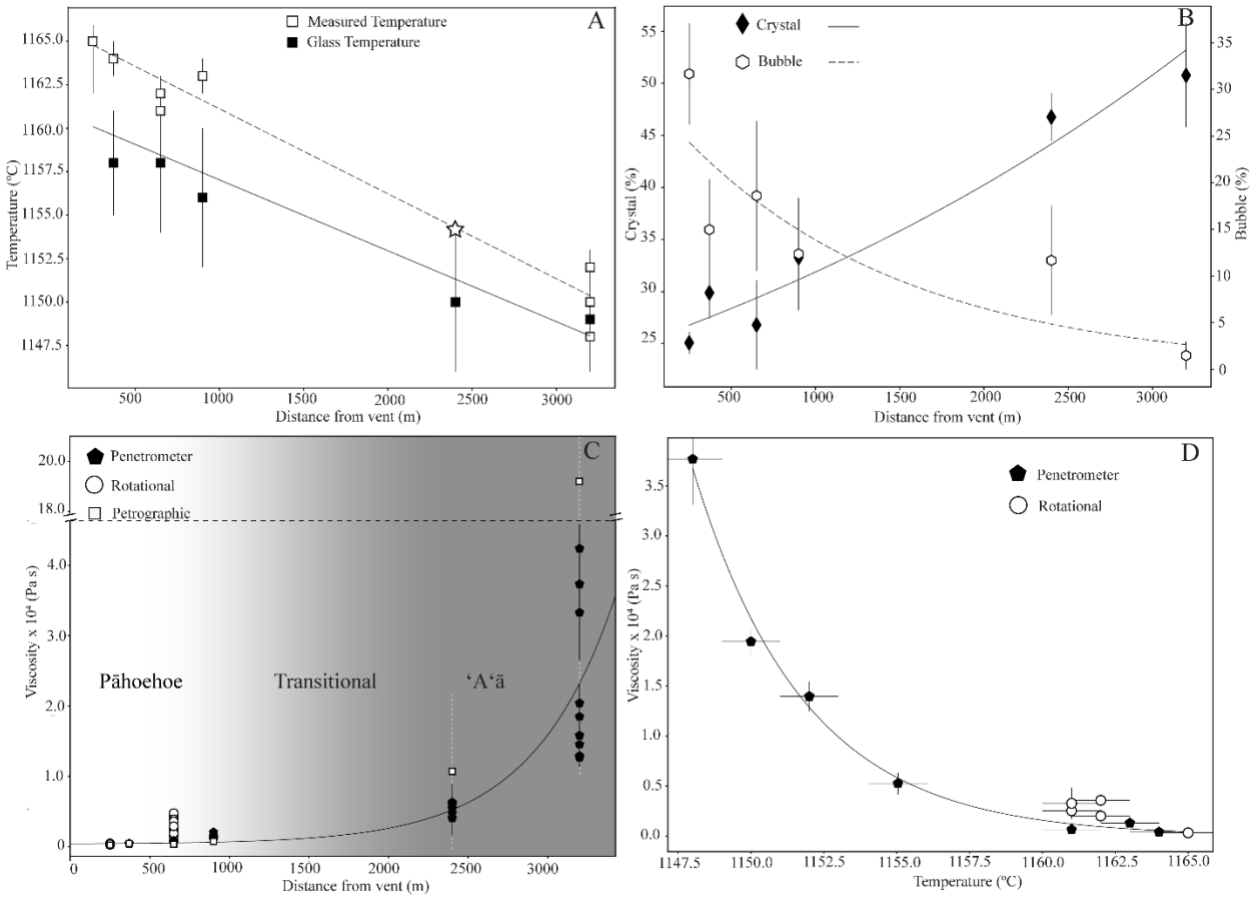


*Figure 3: **Figure 3:** Variation of (A) Temperature (°C), (B) Texture, and (C) viscosity (Pa·s) vs. distance from the vent (m), and (D) viscosity vs. temperature. The star in A is a corrected temperature for Site 5 (see results). For textures (in B), groundmass crystal content (black diamond) (%) is plotted on the left y-axis, and vesicle content (white hexagon) (%) on the right y-axis. Vertical bars represent variations for in situ viscosity (in C and D) and temperature (in A and D) measurements and calculated phase proportions (in B). In C, the dashed grey bars show uncertainties for viscosity obtained from the petrographic model (see S5). Note dashed horizontal line in C denotes a change in y-axis values.*

2021), or by increasing effusion rate or steepening of the flow path, causing higher strain-rates (Keszthelyi et al., 2004; Guilbaud et al., 2005). The Litli-Hrútur effusion rate remained steady throughout all field measurements and lavas spread across a flat valley with no drastic slope changes, therefore changes in strain rate will not have contributed to the pāhoehoe - 'a'ā transition of the Litli-Hrútur lavas, which takes place between Sites 4-5 (Fig. 3C). While vesicularity remains steady between these Sites, crystallinity increases from 33 to 47 %, and temperature decreases from 1163 to 1155 °C, and viscosity changes from 1302 ± 304 to 5311 ± 913 Pa·s. This represents the first *in-situ* measurements that constrain the pāhoehoe - 'a'ā transition zone in active lava (Fig. 3; Table 1). This transition has previously been investigated through morphological, petrological, and experimental studies that propose the transition to take place between 500 to $10^5$ Pa·s at low shear rates (<2 $s^{-1}$) (Hon et al., 2003; Robert et al., 2014; Di Fiore et al., 2021), which broadly agree with our *in-situ* data.

The Ca of Bubbles in all samples is > 3 (S5), and thus bubbles act to decrease the effective viscosity. This is supported by Site 1 pāhoehoe (vesicularity > 30%) having viscosities that are more than 300% lower

than at Site 4 pāhoehoe (vesicularity 12%) (Table 1). We find that while crystallinity increases across the pāhoehoe - 'a'ā transition (~14%), the vesicularity change is minimal (~1%) (Fig. 3B). In contrast, the final large viscosity increase (~5300 to 37000 Pa·s) from rubbly 'a'ā to blocky 'a'ā front (Site 5 to 6), is attributed to a moderate crystallinity increase (~4%) approaching the maximum packing fraction and the near-complete bubble loss in the lava (vesicularity decrease from 12 to 2 %). This suggests that rheological transition zones in three-phase suspensions may be narrower than in two-phase suspensions due to the combined contributions of either phase. This may result in more abrupt changes in eruptive behavior than what the linear combination of two-phase models may predict.

Our *in-situ* data provide the first quantification of viscosity change, and major drivers, during naturally flowing lava. While these exact viscosity values are specific to this eruption, these findings show that *in-situ* techniques improve our understanding of multiphase lava rheology and can help refine existing models that use weighted phase proportions of crystals and vesicles.

### 4.2 Implications for Eruptive Response Protocols

We document the dynamic evolution of temperature, crystallinity, and vesicularity of an active lava flow field with distance and their respective effects on the lava's viscosity (Fig. 3). We compare our *in-situ* data with commonly used three-phase petrographic approaches to deduce lava viscosity (Fig. 3C; S5). This petrographic approach shows a similar trend of viscosity increase with distance. However, as a result of the limitations of models prescribing a rigid maximum packing fraction (*e.g.,* Maron and Pierce, 1956), the uncertainties associated with this approach become extremely large, and it drastically overestimates lava viscosity when the crystal fraction exceeds 50% (*i.e.* Sites 5-6) (Fig. 3C and S5). To deduce these values, we used *in-situ* temperature measurements, which are not always available; using temperatures recovered via MgO glass thermometry would further increase the petrologically derived viscosities. Furthermore, the timescales required to return samples from the field, prepare thin sections, quantify all relevant textural parameters, and obtain melt compositions for this modeling are on the order of days. Additionally, assumptions on relevant strain rates are needed to estimate Ca.

In contrast, *in-situ* viscosity measurements, as we performed here, can be conducted and processed within minutes, and relayed in near-real time to researchers that model lava runout as part of civil protection responses (Chevrel et al., 2022; Harris et al., 2019). Initiation and real-time adjustment of such models with these *in-situ* field viscosity data can greatly increase their accuracy.

## 5. CONCLUSION

We present the first-ever comprehensive real-time, *in-situ* viscosity map of active lava. We measured the viscosity increase along the flow and correlated it to the thermal and textural evolution of the lava. The data show that at high crystal contents, *in-situ* viscosity measurements are significantly lower, and more accurate and precise than values derived from available petrologic approaches. This study highlights that field viscometry is both more precise and faster than what is obtainable with other approaches. Since we provide the first dataset that covers an entire flow, this study marks a starting point for the validation and refinement of experimental and numerical parameterizations of multiphase lava rheology through field viscometry. Additionally, we present the first *in-situ*

constraints of the viscosity range of the pāhoehoe - 'a'ā transition of actively flowing lava. Finally, this *in-situ* methodology can aid global communities as it provides a real-time assessment of lava viscosity that can be implemented into eruptive models used for civil protection.

**ACKNOWLEDGMENTS:** We thank the University of Iceland for its generous support during the field campaign. Funding was provided by the State University of New York at Buffalo Center for Geological and Climate Hazards, National Science Foundation (NSF) EAR RAPID award no. 2241489, and NSF EAR awards no. 2223098 and 2420723. This is contribution 664 from the French Government Laboratory of Excellence Initiative ClerVolc.

[1]Supplemental Material. Item S1: Major-element and glass chemistry of Litli-Hrútur samples, methods, and data tables. Item S2: Combined in situ viscosity and temperature for all measurements conducted in Litli-Hrútur lavas, text, glass thermometry data figure, and data table. Item S3: Calibration for the rotational viscometer, and description of the procedure with a corresponding figure. Item S4: Photomicrographs and textures of Litli-Hrútur samples, methods, and representative figures of lava textures. Item S5: Petrologic approach to modeling three-phase Litli-Hrútur lavas, and data table. Please visit https://doi .org /10 .1130 /GEOL .S.27616911 to access the supplemental material

## REFERENCES CITED

Belousov, A., and Belousova, M., 2018, Dynamics and viscosity of ‘a’a and pahoehoe lava flows of the 2012–2013 eruption of Tolbachik volcano, Kamchatka (Russia): Bulletin of Volcanology, v. 80, doi:10.1007/s00445-017-1180-2.

Cappello, A., Hérault, A., Bilotta, G., Ganci, G., and Del Negro, C., 2016, MAGFLOW: a physics-based model for the dynamics of lava-flow emplacement: Geological Society, London, Special Publications, v. 426, p. 357–373, doi:10.1144/SP426.16.

Cashman, K. V., Thornber, C., and Kauahikaua, J.P., 1999, Cooling and crystallization of lava in open channels, and the transition of Pāhoehoe Lava to ’A’ā: Bulletin of Volcanology, v. 61, p. 306–323, doi:10.1007/s004450050299.

Chevrel, M.O., Harris, A.J.L., James, M.R., Calabrò, L., Gurioli, L., and Pinkerton, H., 2018a, The viscosity of pāhoehoe lava: In situ syn-eruptive measurements from Kilauea, Hawaii: Earth and Planetary Science Letters, v. 493, p. 161–171, doi:https://doi.org/10.1016/j.epsl.2018.04.028.

Chevrel, M.O., Harris, A.J.L., Peltier, A., Villeneuve, N., Coppola, D., Gouhier, M., and Drenne, S., 2022, Volcanic crisis management supported by near real-time lava flow hazard assessment at Piton de la Fournaise, La Réunion: Volcanica, v. 5, p. 313–334, doi:10.30909/vol.05.02.313334.

Chevrel, M.O., Latchimy, T., Batier, L., Delpoux, R., Harris, M.A., and Kolzenburg, S., 2023, A new portable field rotational viscometer for high-temperature melts: Review of Scientific Instruments, v. 94, doi:https://doi.org/10.1063/5.0160247.

Chevrel, M.O., Pinkerton, H., and Harris, A.J.L., 2019, Measuring the viscosity of lava in the field: A review: Earth-Science Reviews, v. 196, doi:10.1016/j.earscirev.2019.04.024.

Costa, A., Caricchi, L., and Bagdassarov, N., 2009, A model for the rheology of particle-bearing suspensions and partially molten rocks: Geochemistry, Geophysics, Geosystems, v. 10, p. 1–13, doi:10.1029/2008GC002138.

Costa, A., and Macedonio, G., 2005, Computational modeling of lava flows: A review, *in* Manga, M. and Ventura, G. eds., Kinematics and dynamics of lava flows, Geological Society of America, v. 396, p. 0, doi:10.1130/0-8137-2396-5.209.

Dietterich, H.R., Diefenbach, A.K., Soule, S.A., Zoeller, M.H., Patrick, M.P., Major, J.J., and Lundgren, P.R., 2021, Lava effusion rate evolution and erupted volume during the 2018 Kīlauea lower East Rift Zone eruption: Bulletin of Volcanology, v. 83, doi:10.1007/s00445-021-01443-6.

Di Fiore, F., Vona, A., Kolzenburg, S., Mollo, S., and Romano, C., 2021, An Extended Rheological Map of Pāhoehoe—ʻAʻā Transition: Journal of Geophysical Research: Solid Earth, v. 126, p. 1–23, doi:10.1029/2021JB022035.

Fink, J.H., and Zimbelman, J., 1990, Longitudinal Variations in Rheological Properties of Lavas: Puu Oo Basalt Flows, Kilauea Volcano, Hawaii, *in* IAVCEI Proceedings in Volcanology, p. 157–173, doi:10.1007/978-3-642-74379-5_7.

Guilbaud, M.N., Self, S., Thordarson, T., and Blake, S., 2005, Morphology, surface structures, and emplacement of lavas produced by Laki, A.D. 1783-1784: Special Paper of the Geological Society of America, v. 396, p. 81–102, doi:10.1130/0-8137-2396-5.81.

Harris, A.J.L. et al., 2019, Validation of an integrated satellite-data-driven response to an effusive crisis: The april-may 2018 eruption of piton de la fournaise: Annals of Geophysics, v. 62, doi:10.4401/ag-7972.

Harris, M.A., Kolzenburg, S., Sonder, I., and Chevrel, M.O., 2024, A new portable penetrometer for measuring the viscosity of active lava: Review of Scientific Instruments, v. 95, p. 65103, doi:10.1063/5.0206776.

Harris, A.J.L., and Rowland, S.K., 2001, Kinematic Thermo-rheological model for lava cooling in a channel: Bulletin of Volcanology, v. 63, p. 20–44.

Hon, K., Gansecki, C., and Kauahikaua, J., 2003, The transition from ʻa'ā to pāhoehoe crust on 282 flows emplaced during the Pu'u 'Ō'ō–Kūpaianaha eruption, *in* Heliker, C., Swanson, D.A., 283 and Takahashi, T.J., eds., The Puʻu ʻŌʻō-Kūpaianaha Eruption of Kīlauea Volcano, Hawaiʻi: 284 The First 20 Years: U.S. Geological Survey Professional Paper 1676, p. 89–103, 285 https://pubs.usgs.gov/pp/pp1676/pp1676_05.pdf.

Hyman, D.M.R., Dietterich, H.R., and Patrick, M.R., 2022, Toward Next-Generation Lava Flow Forecasting: Development of a Fast, Physics-Based Lava Propagation Model: Journal of Geophysical Research: Solid Earth, v. 127, p. 1–27, doi:10.1029/2022JB024998.

James, M.R., Bagdassarov, N., Müller, K., and Pinkerton, H., 2004, Viscoelastic behaviour of basaltic lavas: Journal of Volcanology and Geothermal Research, v. 132, p. 99–113, doi:10.1016/S0377-0273(03)00340-8.

Keszthelyi, L., Thordarson, T., McEwen, A., Haack, H., Guilbaud, M.N., Self, S., and Rossi, M.J., 2004, Icelandic analogs to Martian flood lavas: Geochemistry, Geophysics, Geosystems, v. 5, doi:10.1029/2004GC000758.

Kolzenburg, S., Chevrel, M.O., and Dingwell, D.B., 2022, Magma / Suspension Rheology: Reviews in Mineralogy and Geochemistry, v. 87, p. 639–720, doi:10.2138/rmg.2022.87.14.

Krmíček, L., Troll, V.R., Thordarson, T., Brabec, M., Moreland, W.M., and Maťo, A., 2023a, The 2023 Litli-Hrútur eruption of the Fagradalsfjall Fires, SW-Iceland: Insights from trace element compositions of olivine: Czech Polar Reports, v. 13, p. 257–270,

doi:10.5817/CPR2023-2-20.
Lev, E., and James, M.R., 2014, The influence of cross-sectional channel geometry on rheology and flux estimates for active lava flows: Bulletin of Volcanology, v. 76, p. 1–15, doi:10.1007/s00445-014-0829-3.
Mader, H.M., Llewellin, E.W., and Mueller, S.P., 2013, The rheology of two-phase magmas: A review and analysis: Journal of Volcanology and Geothermal Research, v. 257, p. 135–158, doi:10.1016/j.jvolgeores.2013.02.014.
Maron, S.H., and Pierce, P.E., 1956, Application of ree-eyring generalized flow theory to suspensions of spherical particles: Journal of Colloid Science, v. 11, p. 80–95, doi:https://doi.org/10.1016/0095-8522(56)90023-X.
Moore, H.J., 1987, Preliminary estimates of the rheological properties of 1984 Mauna Loa lava, 313 *in* Decker, R.W., Wright, T.L., and Stauffer, P.H., eds., Volcanism in Hawaii: U.S. Geological Survey Professional Paper 1350, p. 1569–1588, 315 https://pubs.usgs.gov/pp/1987/1350/pdf/chapters/pp1350_ch58.pdf.
Pankhurst, M.J. et al., 2022, Rapid response petrology for the opening eruptive phase of the 2021 Cumbre Vieja eruption, La Palma, Canary Islands: Volcanica, v. 5, p. 1–10, doi:10.30909/vol.05.01.0110.
Pinkerton, H., and Sparks, R.S.J., 1978, Field measurements of the rheology of lava: Nature, v. 276, p. 383–385, doi:10.1038/276383a0.
Robert, B., Harris, A., Gurioli, L., Médard, E., Sehlke, A., and Whittington, A., 2014, Textural and rheological evolution of basalt flowing down a lava channel: Bulletin of Volcanology, v. 76, p. 1–21, doi:10.1007/s00445-014-0824-8.
Thordarson, T. et al., 2023, The 2021, 2022, and 2023 eruptions of Fagradalsfjall Fires, Reykjanes Peninsula Iceland, *in* American Geophysical Union Fall Meeting, p. V32A-02.
Wieser, P., Petrelli, M., Lubbers, J., Wieser, E., Ozaydin, S., Kent, A., and Till, C., 2022, Thermobar: An open-source Python3 tool for thermobarometry and hygrometry: Volcanica, v. 5, p. 349–384, doi:10.30909/vol.05.02.349384.

Harris, M.A., et al., 2024, Real-time, in situ viscosity mapping of active lava: Geology, https://doi.org/10.1130/G52558.1

# Supplemental Material

Item S1: Major-element and glass chemistry of Litli-Hrútur samples, methods, and data tables. Item S2: Combined in situ viscosity and temperature for all measurements conducted in Litli-Hrútur lavas, text, glass thermometry data figure, and data table. Item S3: Calibration for the rotational viscometer, and description of the procedure with a corresponding figure. Item S4: Photomicrographs and textures of Litli-Hrútur samples, methods, and representative figures of lava textures. Item S5: Petrologic approach to modeling three-phase Litli-Hrútur lavas, and data table.

# *Supplementary Materials: In-situ* viscosity mapping of the 2023 Litli Hrútur lavas, Iceland

M.A. Harris[1,a], M.O. Chevrel[1,2,3,4] , J.T. Parsons[1], T. Latchimy[2] , T. Thordarson[5], A. Höskuldsson[6], W.M. Moreland[5], M. Payet—Clerc[3,5], S. Kolzenburg[1]

*[1]Department of Geology, University at Buffalo, 126 Cooke Hall Buffalo, NY 14260-4130, USA*
*[2]Université Clermont Auvergne, CNRS, IRD, OPGC, Laboratoire Magmas et Volcans, 63000 Clermont-Ferrand, France.*
*[3]Université Paris Cité, Institut de physique du globe de Paris, CNRS, 75005 Paris, France*
*[4]Observatoire volcanologique du Piton de la Fournaise, Institut de physique du globe de Paris, 97418 La Plaine des Cafres, France*
*[5]Faculty of Earth Sciences, University of Iceland, Sturlugata 7, IS-102 Reykjavík, Iceland*
*[6] Nordic Volcanological Centre, Institute of Earth Sciences, University of Iceland, Sturlugata 7, IS-102 Reykjavík, Iceland*

**S1: Major Element and Glass Chemistry of Litli Hrútur Samples**

Major element and glass geochemical analyses were conducted at the Laboratoire Magmas and Volcans, Université Clermont Auvergne, France. Whole-rock major element chemistry was conducted with Inductively coupled plasma-optical emission spectrometry (ICP-OES) and the results are reported in Table S1.1 as oxide values. The chemical composition of the glassy matrix of each sample was measured on polished thin sections via electron microprobe CAMECA SX 100 (at 15 kV and a defocused beam of 20 μm at a current of 8 nA for glass and a focused beam at 15 nA for minerals), they are reported as averaged values of n number of analyses in Table S1.2.

| Site | Sample name | UTM E | UTM N | SiO2 | Al2O3 | FeO (Total) | MgO | CaO | Na2O | K2O | TiO2 | MnO | P2O5 | Ba | Sr | H2O+ | H2O- | Total |
|---|---|---|---|---|---|---|---|---|---|---|---|---|---|---|---|---|---|---|
| 1 | 19-06 | 440846 | 7088729 | 48.9 | 16.12 | 10.69 | 8.41 | 12.96 | 1.91 | 0.28 | 1.13 | 0.16 | 0.12 | 0.0075 | 0.0152 | 0.07 | 0.7 | 100.0 |
| 2 | 23-01 | 440626 | 7088462 | 49.12 | 16.28 | 10.65 | 8.54 | 12.98 | 1.94 | 0.28 | 1.13 | 0.16 | 0.13 | 0.0076 | 0.0154 | 0.07 | 0.8 | 100.5 |
| 3 | 25-09 | 441154 | 7087999 | 49.23 | 16.49 | 10.65 | 8.49 | 13.02 | 1.94 | 0.28 | 1.12 | 0.16 | 0.13 | 0.0076 | 0.0155 | 0.06 | 0.78 | 100.8 |
| 4 | 20-06 | 440551 | 7087877 | 48.83 | 16.34 | 10.46 | 8.4 | 12.98 | 1.9 | 0.26 | 1.1 | 0.16 | 0.13 | 0.0072 | 0.0152 | 0.06 | 0.64 | 100.0 |
| 5 | 17-02 | 440625 | 7086421 | 48.98 | 16.39 | 10.31 | 8.43 | 13.00 | 1.92 | 0.27 | 1.09 | 0.16 | 0.12 | 0.0073 | 0.0152 | 0.09 | 0.77 | 100.0 |
| 6 | 25-04 | 439971 | 7085528 | 48.59 | 16.29 | 10.43 | 8.44 | 12.99 | 1.91 | 0.29 | 1.09 | 0.16 | 0.12 | 0.0074 | 0.0151 | 0.06 | 0.65 | 99.8 |
| | 2σ% | | | 0.19 | 0.21 | 0.36 | 0.15 | 0.14 | 0.04 | 0.03 | 0.09 | 0.01 | 0.02 | 0.002 | 0.004 | 0 | 0 | |

Table S1.1: Whole Rock Major Element Chemistry

| Site | Sample name | UTM E | UTM N | SiO2 | Al2O3 | FeO (Total) | MgO | CaO | Na2O | K2O | TiO2 | MnO | P2O5 | N= | Total |
|---|---|---|---|---|---|---|---|---|---|---|---|---|---|---|---|
| 1 | 19-03 | 440846 | 7088729 | 49.38 | 13.72 | 10.77 | 7.38 | 12.91 | 1.96 | 0.37 | 1.52 | 0.20 | 0.17 | 15 | 98.39 |
| 2 | 23-01 | 440626 | 7088462 | 49.35 | 13.49 | 11.60 | 7.05 | 12.44 | 2.06 | 0.42 | 1.66 | 0.21 | 0.21 | 13 | 98.50 |
| 3 | 25-09 | 441154 | 7087999 | 49.38 | 13.52 | 11.74 | 7.06 | 12.23 | 2.06 | 0.44 | 1.71 | 0.22 | 0.20 | 18 | 98.54 |
| 4 | 20-01 | 440551 | 7087877 | 49.23 | 13.37 | 11.76 | 6.95 | 12.16 | 2.08 | 0.43 | 1.69 | 0.21 | 0.18 | 13 | 98.06 |
| 5 | 17-02 | 440625 | 7086421 | 49.47 | 13.14 | 12.52 | 6.65 | 11.76 | 2.13 | 0.48 | 1.86 | 0.21 | 0.22 | 26 | 98.45 |
| 6 | 25-05 | 439971 | 7085528 | 49.38 | 13.04 | 12.26 | 6.59 | 11.75 | 2.13 | 0.48 | 1.88 | 0.21 | 0.24 | 25 | 97.97 |
| | 2σ% | | | 0.27 | 0.10 | 0.18 | 0.12 | 0.11 | 0.06 | 0.02 | 0.02 | 0.05 | 0.04 | | |

Table S1.2: Electron Microprobe Glass Chemistry

## S2: Combined *in-situ* viscosity and temperature measurements conducted in Litli Hrútur lavas.

Although the rotational viscometer (RV) is equipped with a K-type thermocouple (1mm thick), thermocouple failure through shear forces and data transmission problems restricted stable readings, and hence temperature from the RV was only obtained at Site 1. All other thermocouple temperatures reported are from *in-situ* measurements with a separate thermoprobe involving 3mm thick K-Type thermocouples fastened to a steel rod and a multichannel data logger. We were unable to obtain stable in-situ thermal readings for the Site 5 lavas, thus the glass temperature for this site corrected by the systematic offset of ~5℃ is used instead).

Lava flowing in open channels cools significantly during transport, causing increased crystallization and viscosity, affecting the flow distance (Cashman et al., 1999; Harris and Rowland, 2001; Kolzenburg et al., 2016). We find a slight difference between the measured *in-*

*situ* cooling rate (4.9°C/km) and the one recovered via glass thermometry (4.1 °C/km) (Fig. 3A and). This suggests that glass thermometry may be affected by a lag in magnesium diffusion at the time of quenching, leading to an underestimate of lava temperature but it remains valuable for determining cooling rates. Both measured and petrologically determined cooling rates are similar to those observed at comparably sized eruptions in Hawaii (Cashman et al., 1999; Robert et al., 2014, Chevrel et al. 2018a) and Iceland (Kolzenburg et al., 2017).

Table S2: All Viscosity, Temperature, and Distance data for the Litli Hrútur Eruption

| Site # | Run# | Viscosity (Pa s) | 2σ | Thermocouple Temperature (°C) | Glass Temperature* (°C) | 2σ | Distance From Vent (m) | Date of Measuremnt |
|---|---|---|---|---|---|---|---|---|
| 1[a] | RV1 | 255 | 118 | 1165 | 1165 | 3 | 250 | 19/07/2024 |
| 1[a] | RV2 | 245 | 57 | 1165 | 1165 | 3 | 250 | 19/07/2024 |
| 1[a] | RV3 | 449 | 95 | 1165 | 1165 | 3 | 250 | 19/07/2024 |
| 1[a] | RV4 | 341 | 37 | 1165 | 1165 | 3 | 250 | 23/07/2024 |
| 2 | LP15 | 365 | 215 | 1164 | 1158 | 3 | 370 | 23/07/2024 |
| 2 | LP16 | 433 | 206 | 1164 | 1158 | 3 | 370 | 23/07/2024 |
| 3[1] | RV5 | 2462 | 1386 | 1161 | 1158 | 3 | 650 | 25/07/2024 |
| 3[1] | RV6 | 2582 | 1285 | 1161 | 1158 | 3 | 650 | 25/07/2024 |
| 3[1] | RV7 | 4334 | 141 | 1161 | 1158 | 3 | 650 | 25/07/2024 |
| 3[1] | RV8 | 4755 | 144 | 1161 | 1158 | 3 | 650 | 25/07/2024 |
| 3[1] | RV9 | 2550 | 120 | 1161 | 1158 | 3 | 650 | 25/07/2024 |
| 3[1] | LP26 | 810 | 386 | 1161 | 1158 | 4 | 650 | 25/07/2024 |
| 3[1] | LP27 | 431 | 242 | 1161 | 1158 | 4 | 650 | 25/07/2024 |
| 3[1] | LP28 | 727 | 366 | 1161 | 1158 | 4 | 650 | 25/07/2024 |
| 3[1] | LP29 | 788 | 260 | 1161 | 1158 | 4 | 650 | 25/07/2024 |
| 3[1] | LP30 | 596 | 233 | 1161 | 1158 | 4 | 650 | 25/07/2024 |
| 3[1] | LP31 | 508 | 310 | 1161 | 1158 | 4 | 650 | 25/07/2024 |
| 3[1] | RV10 | 1444 | 719 | 1161 | 1158 | 3 | 650 | 26/07/2024 |
| 3[2] | RV11 | 2779 | 342 | 1162 | - | - | 650 | 26/07/2024 |
| 3[2] | RV12 | 3837 | 66 | 1162 | - | - | 650 | 26/07/2024 |
| 3[2] | RV13 | 3772 | 685 | 1162 | - | - | 650 | 26/07/2024 |
| 3[2] | RV14 | 3879 | 183 | 1162 | - | - | 650 | 26/07/2024 |
| 3[2] | RV15 | 3591 | 354 | 1162 | - | - | 650 | 26/07/2024 |
| 3[2] | RV16 | 1800 | 35 | 1162 | - | - | 650 | 26/07/2024 |
| 3[2] | RV17 | 1469 | 247 | 1162 | - | - | 650 | 26/07/2024 |
| 3[2] | RV18 | 1870 | 458 | 1162 | - | - | 650 | 26/07/2024 |
| 3[2] | RV19 | 2891 | 804 | 1162 | - | - | 650 | 26/07/2024 |
| 4 | LP6 | 2034 | 248 | 1163 | 1156 | 4 | 900 | 20/07/2024 |
| 4 | LP7 | 1161 | 146 | 1163 | 1156 | 4 | 900 | 20/07/2024 |
| 4 | LP8 | 1025 | 199 | 1163 | 1156 | 4 | 900 | 20/07/2024 |
| 4 | LP9 | 1101 | 110 | 1163 | 1156 | 4 | 900 | 20/07/2024 |
| 4 | LP10 | 1503 | 198 | 1163 | 1156 | 4 | 900 | 20/07/2024 |
| 4 | LP11 | 1203 | 171 | 1163 | 1156 | 4 | 900 | 20/07/2024 |
| 4 | LP12 | 1258 | 113 | 1163 | 1156 | 4 | 900 | 20/07/2024 |

| | | | | | | | | |
|---|---|---|---|---|---|---|---|---|
| 4 | LP13 | 1216 | 197 | 1163 | 1156 | 4 | 900 | 20/07/2024 |
| 4 | LP14 | 1214 | 355 | 1163 | 1156 | 4 | 900 | 20/07/2024 |
| 5 | LP1 | 4787 | 2551 | - | 1150 | 4 | 2400 | 17/07/2024 |
| 5 | LP2 | 5470 | 1207 | - | 1150 | 4 | 2400 | 17/07/2024 |
| 5 | LP3 | 5980 | 950 | - | 1150 | 4 | 2400 | 17/07/2024 |
| 5 | LP4 | 6287 | 2565 | - | 1150 | 4 | 2400 | 17/07/2024 |
| 5 | LP5 | 4033 | 2424 | - | 1150 | 4 | 2400 | 17/07/2024 |
| 6 | LP17 | 18480 | 2598 | 1150 | 1149 | 3 | 3200 | 25/07/2024 |
| 6 | LP18 | 20397 | 2672 | 1150 | 1149 | 3 | 3200 | 25/07/2024 |
| 6 | LP19 | 42401 | 3498 | 1148 | 1149 | 3 | 3200 | 25/07/2024 |
| 6 | LP20 | 33293 | 6829 | 1148 | 1149 | 3 | 3200 | 25/07/2024 |
| 6 | LP21 | 37344 | 4546 | 1148 | 1149 | 3 | 3200 | 25/07/2024 |
| 6 | LP22 | 15807 | 1774 | 1152 | 1149 | 3 | 3200 | 25/07/2024 |
| 6 | LP23 | 12898 | 1519 | 1152 | 1149 | 3 | 3200 | 25/07/2024 |
| 6 | LP24 | 14506 | 3054 | 1152 | 1149 | 3 | 3200 | 25/07/2024 |
| 6 | LP25 | 12641 | 1069 | 1152 | 1149 | 3 | 3200 | 25/07/2024 |

Thermocouple (K-Type) uncertainty is ± 1℃. Site $1^{a}$ = Temperatures from *in*-situ thermocouple of RV. $3^{1}$ = Measurements conducted at Site 3 on 25 July 2023, $3^{2}$ = Measurements conducted at Site 3 on 26 July 2023
*Glass thermometry calculation after Helz and Thornber, (1987).

## S3: Calibration for the rotational viscometer

Calibrating the rotational viscometer has been carried out for three shear-vanes sizes: 1) 80 mm length and 25 mm radius (SV 80-25), 2) 60 mm length and 20 mm radius (SV 60-20), and 3) 30 mm length and 15 mm radius (SV 30-15). Instead of defining the relationship between viscosity and torque for each rotational speed, as done in (Chevrel et al., 2023), we here define the relationship between viscosity and the ratio of torque divided by the rotational velocity.

Best fits were obtained using a polynomial function:

$$\eta = A(\frac{M}{RPM)})^2 + B\left(\frac{M}{RPM)}\right) + C$$

Where M is the torque (given in mN·m by the instrument) and RPM is the applied rotational speed (in revolutions per minute).

Parameters A, B, and C are determined for each shear vane over a speed range from 2 to 100 RPM and torques from 10 to 2500 mN.m (Fig S3A).

Calibrations were conducted between 11°C and 60°C using an N190000© Cannon standard Oil corresponding to a viscosity range between 30 and 4300 Pa s. Viscosity outside of the calibrated temperature provided by Cannon was obtained from the non-arrhenian viscosity-temperature correlation provided by Harris et al., (2024), which is based on carefully calibrated concentric cylinder viscometry measurements. Additional experiments were conducted with the N15000© Cannon standard Oil at 24°C and 34°C and viscosity of 44 and 18 Pa s.

These equations allow us to retrieve the viscosity within an error of a maximum of 10 % (Fig S3B).

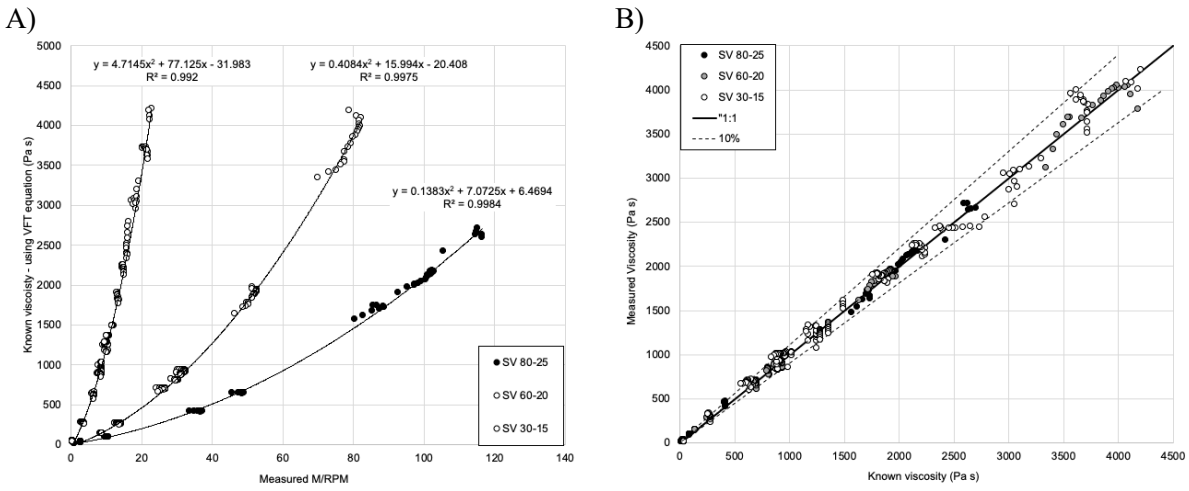


Figure S3: A) Calibration curve and equation for each shear-vane; B) Measured viscosity using the calibration versus the certified known viscosity. Black line is the 1:1 relationship and the dashed lines represent the 10% envelope.

**S4: Photomicrographs and Textures of Litli Hrútur Samples**

Two to three thin sections of lava samples quenched at each site were analyzed with optical and scanning electron microscopy (SEM) at the University at Buffalo shared facilities center (Hitachi S4000). All reported data on crystal abundances report post-eruptive groundmass crystallinity (200μm to 10μm) (Fig. S4.1) to track the syn-emplacement crystallization of the lava. Four photomicrographs (70x-500x magnification) of each site were manipulated to convert to gray-scale, remove cracks and non-groundmass cargo, and then processed with ImageJ (*e.g.,* Schneider et al., 2012) to determine crystal area fraction. A similar method was used for bubbles: two to three full thin-section scans (~25x40mm) for each site. Additional manual tracing of bubble outlines was done before processing in ImageJ with a minimum vesicle size of 100μm (Fig. S4.2).

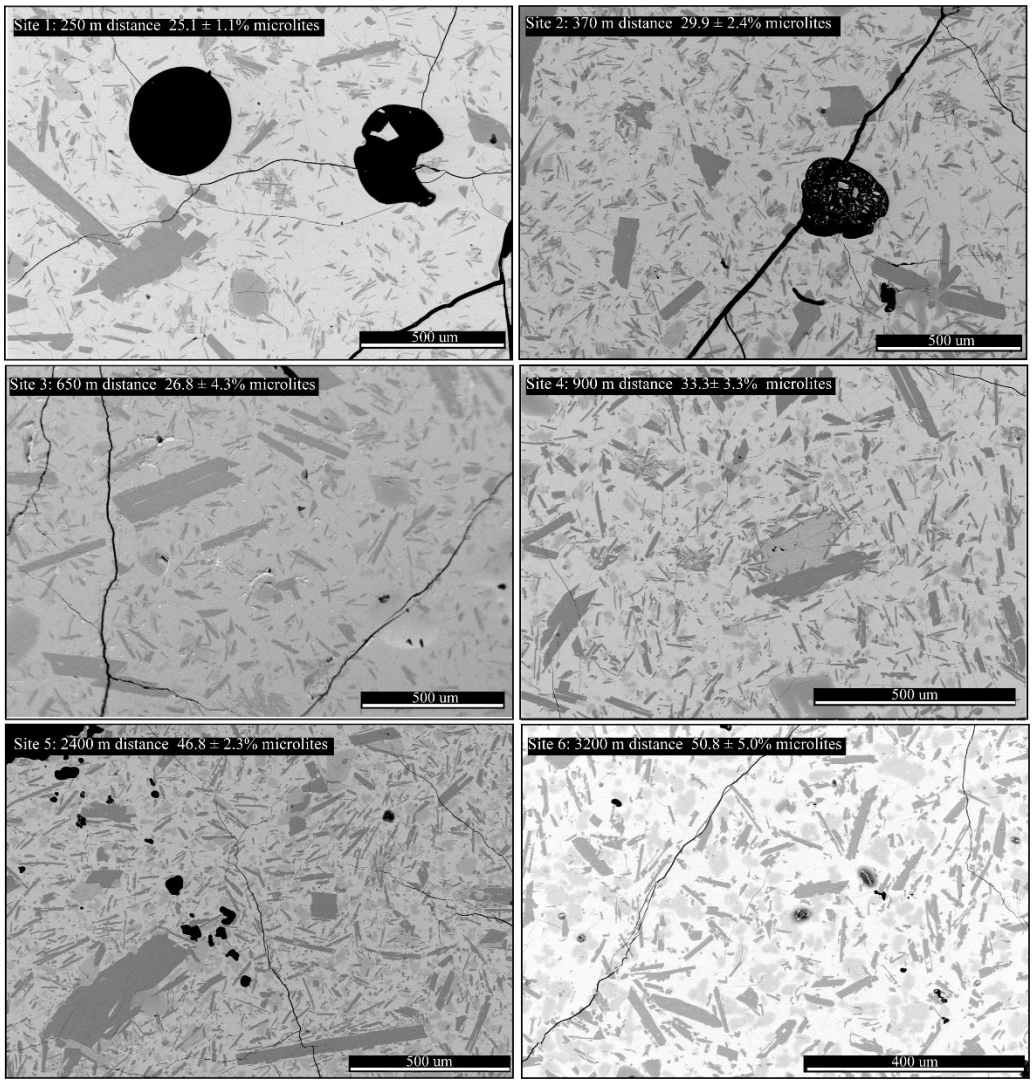


Figure S4.1: Six representative SEM photomicrographs for Litli Hrútur lavas, showing backscatter imagery of groundmass crystals. Coarse phenocrysts, cracks, and vesicles were excluded from the images before analysis with ImageJ.

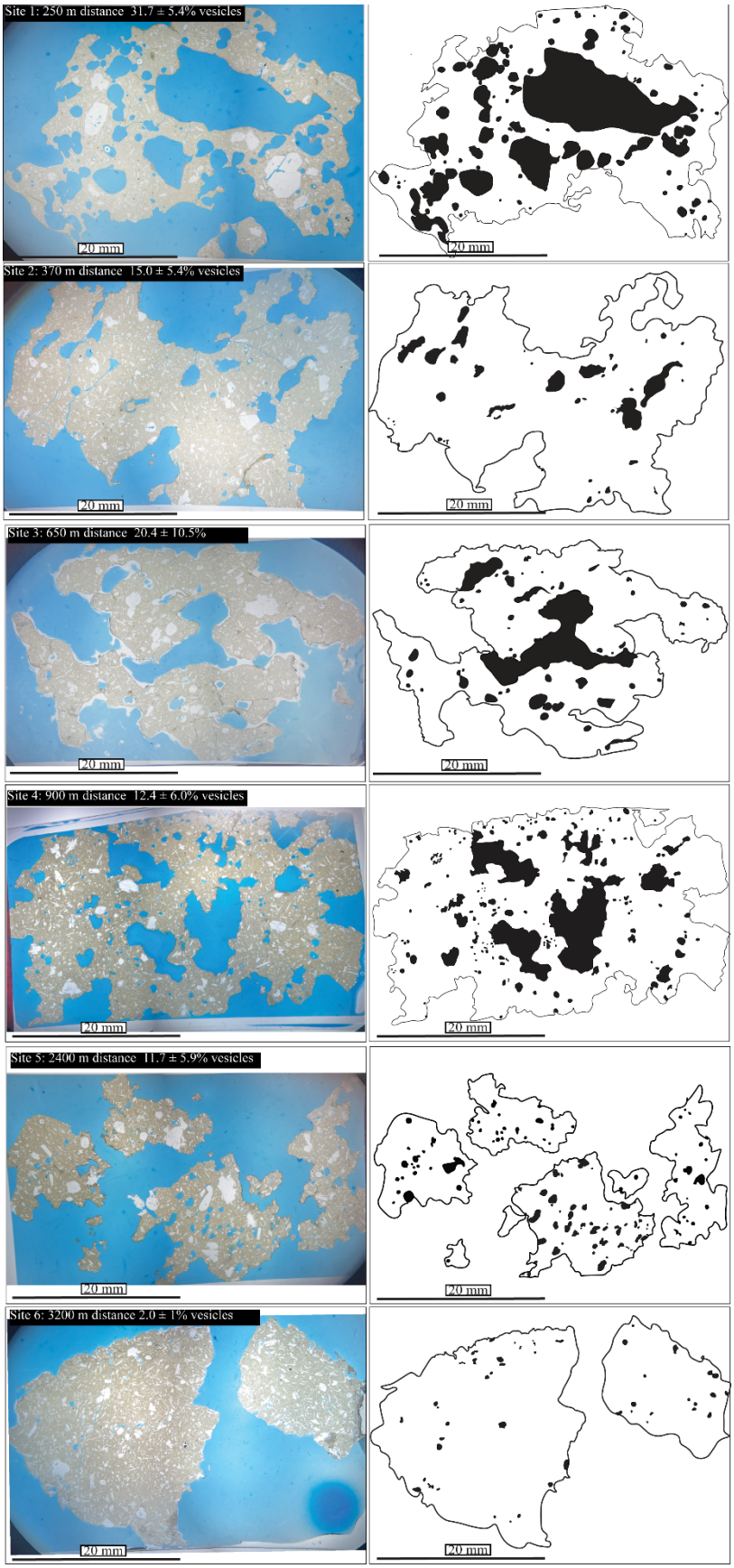


Figure S4.2: Six representative plain-light photomicrographs for Litli Hrútur lavas and respective traced vesicle renderings used for area % analyses with ImageJ. Thin sections were prepared with blue epoxy to facilitate vesicle identification.

**S5: Petrologic approach to modeling three-phase Litli Hrútur lavas.**

We apply a simple petrologic approach to model the three-phase viscosity of the Litli Hrútur lavas based on their recovered glass chemistries and the volumetric fractions of crystals (($\Phi c$) and bubbles ($\Phi b$). The single-phase liquid (melt) viscosity for each representative site was determined using the major element glass chemical analyses (S1) as input to the viscosity model of Giordano et al., (2008), evaluated at the *in-situ* temperatures measured at each site rather than the less representative glass temperatures calculated with Thermobar. Values of 0.002 $H_2O$ % were input for each sample, as these estimates are consistent with average values reported by Bindeman et al., (2022) for earlier Fagradalsfjall eruptions. We calculate the effective viscosity of the particle suspension ($\eta_{rc}$) based on a monodisperse maximum packing fraction ( $\Phi m$ ) of rough particles (e.g., Mader et al., 2013), and the average aspect ratio of the crystals determined at each site via ImageJ analyses of thin-section photomicrographs.

We employ, the modified Maron and Pierce, (1956) equation:

$$\eta_{rc} = (1 - \frac{\Phi c}{\Phi m})^{-2}$$

Combined with the melt viscosity to yield the effective viscosity of a two-phase medium (melt+crystal) suspension that describes the textural state of the sample at each site (Table S5).

This liquid+crystalsuspension is then treated as the effective medium for a bubble suspension, where the effect of bubbles on the particle suspension was then determined as relative bubble suspension viscosity $\eta_{rb}$ for the high capillary number regime (Ca >1), where bubbles are deformable after Llewellin and Manga, (2005):

$$\eta_{rb} = (1 - \Phi b)^{5/3}$$

For these calculations, the mean bubble radius was recovered from ImageJ and hand sample analyses and used to determine the capillary number following (Mader et al., 2013). Note that this was done assuming monodisperse bubble distribution as no current model exists to address polydisperse bubbles. We use a strain rate of 0.5 $s^{-1}$ based on approximate lava flow field dimensions (e.g., Kolzenburg et al., 2018) and assume a bubble relaxation timescale as:

$$\lambda = \frac{\eta_{melt+crystal} a}{\Gamma}$$

Where $\eta_{melt+crystal}$ is the viscosity of the effective medium (melt+crystal), $a$ is the bubble radius, and Γ is bubble surface tension (0.3 $Nm^{-1}$) (Mader et al., 2013 and references therein).

The final three-phase viscosity was determined based on the effective medium theory (i.e., Phan-Thien and Pham, 1997) where the effect of each phase (melt, crystals, and bubbles) is combined as:

$$\eta_{eff} = \eta_{melt} \times \eta_{rc} \times \eta_{rb}$$

And yield an empirical, petrologically derived three-phase viscosity (Table S5).

We report the uncertainty ranges for single, two-, and three-phase modeling results in Table S5. These were determined by implementing combinations of minimum and maximum temperatures and phase proportions within each respective model that return the maximum and minimum effective viscosity for each site. These are shown as dashed lines in Fig. 3C. We note that the extremely large uncertainties associated with the petrological models at high crystal fractions (Site 5-6) are an inherent part of the limitations of the approach. Our comparison of petrologic results with *in-situ* results in Fig. 3C emphasizes the benefits of employing field rheology techniques to rapid eruption protocols as they can yield faster results with significantly less uncertainty than the petrologic techniques.

**Table S5**: Parameters for Petrologocial modeling of Litli Hrútur lavas

| | Temperature (°C) | Aspect Ratio | Mean Bubble Diameter | Melt viscosity[1] (Pa s) | Uncertainty Range | Melt + crystal viscosity[2] (Pa s) | Uncertainty Range | Melt + crystal + bubble viscosity[3] (Pa s) | Uncertainty Range | Ca[4] |
|---|---|---|---|---|---|---|---|---|---|---|
| Site 1 | 1165 | 3 | 10 | 97 | 17 | 401 | 31 | 211 | 43 | 3 |
| Site 2 | 1164 | 2 | 10 | 107 | 19 | 581 | 96 | 443 | 122 | 5 |
| Site 3 | 1161 | 2 | 10 | 113 | 12 | 479 | 95 | 337 | 184 | 4 |
| Site 4 | 1163 | 2.5 | 10 | 113 | 20 | 916 | 244 | 740 | 356 | 8 |
| Site 5 | 1155* | 2 | 3 | 148 | 28 | 13232 | 6072 | 10693 | 11975 | 33 |
| Site 6 | 1150 | 2 | 2 | 176 | 35 | 198576 | 187307 | 192002 | 181290 | 331 |

[1] Liquid viscosity determined from major element glass chemical analyses applied with Giordano et al., (2008).
[2] Two-phase viscosity calculated for rough particles after Mader et al., (2013) and particle effective viscosity from Maron and Pierce, (1956).
[3] Three-phase viscosity was calculated using effective medium theory (Phan-Thien and Pham, 1997) as the product of the two-phase viscosity and the effective viscosity of the elongated bubbles based on Llewellin and Manga, (2005).
[4]Capillary number at a strain rate of 0.5 $s^{-1}$ (Mader et al., 2013)

Supplementary References:

Bindeman, I.N., Deegan, F.M., Troll, V.R., Thordarson, T., Höskuldsson, Moreland, W.M., Zorn, E.U., Shevchenko, A. V., and Walter, T.R., 2022, Diverse mantle components with invariant oxygen isotopes in the 2021 Fagradalsfjall eruption, Iceland: Nature Communications, v. 13, p. 1–12, doi:10.1038/s41467-022-31348-7.

Cashman, K. V., Thornber, C., and Kauahikaua, J.P., 1999, Cooling and crystallization of lava in open channels, and the transition of Pāhoehoe Lava to ’A’ā: Bulletin of Volcanology, v. 61, p. 306–323, doi:10.1007/s004450050299.

Chevrel, M.O., Latchimy, T., Batier, L., Delpoux, R., Harris, M.A., and Kolzenburg, S., 2023, A new portable field rotational viscometer for high-temperature melts: Review of Scientific Instruments, v. 94, doi:https://doi.org/10.1063/5.0160247.

Giordano, D., Russell, J.K., and Dingwell, D.B., 2008, Viscosity of magmatic liquids: A model: Earth and Planetary Science Letters, v. 271, p. 123–134, doi:10.1016/j.epsl.2008.03.038.

Harris, M.A., Kolzenburg, S., Sonder, I., and Chevrel, M.O., 2024, A new portable penetrometer

for measuring the viscosity of active lava: Review of Scientific Instruments, v. 95, p. 65103, doi:10.1063/5.0206776.
Harris, A.J.L., and Rowland, S.K., 2001, Kinematic Thermo-rheological model for lava cooling in a channel: Bulletin of Volcanology, v. 63, p. 20–44.
Helz, R.T., and Thornber, C.R., 1987, Geothermometry of Kilauea Iki lava lake, Hawaii: Bulletin of Volcanology, v. 49, p. 651–668, doi:10.1007/BF01080357.
Kolzenburg, S., Giordano, D., Cimarelli, C., and Dingwell, D.B., 2016, In situ thermal characterization of cooling/crystallizing lavas during rheology measurements and implications for lava flow emplacement: Geochimica et Cosmochimica Acta, v. 195, p. 244–258, doi:10.1016/j.gca.2016.09.022.
Kolzenburg, S., Giordano, D., Hess, K.U., and Dingwell, D.B., 2018, Shear Rate-Dependent Disequilibrium Rheology and Dynamics of Basalt Solidification: Geophysical Research Letters, v. 45, p. 6466–6475, doi:10.1029/2018GL077799.
Kolzenburg, S., Giordano, D., Thordarson, T., Höskuldsson, A., and Dingwell, D.B., 2017, The rheological evolution of the 2014/2015 eruption at Holuhraun, central Iceland: Bulletin of Volcanology, v. 79, doi:10.1007/s00445-017-1128-6.
Llewellin, E.W., and Manga, M., 2005, Bubble suspension rheology and implications for conduit flow: Journal of Volcanology and Geothermal Research, v. 143, p. 205–217, doi:10.1016/j.jvolgeores.2004.09.018.
Mader, H.M., Llewellin, E.W., and Mueller, S.P., 2013, The rheology of two-phase magmas: A review and analysis: Journal of Volcanology and Geothermal Research, v. 257, p. 135–158, doi:10.1016/j.jvolgeores.2013.02.014.
Maron, S.H., and Pierce, P.E., 1956, Application of ree-eyring generalized flow theory to suspensions of spherical particles: Journal of Colloid Science, v. 11, p. 80–95, doi:https://doi.org/10.1016/0095-8522(56)90023-X.
Phan-Thien, N., and Pham, D.C., 1997, Differential multiphase models for polydispersed suspensions and particulate solids: Journal of Non-Newtonian Fluid Mechanics, v. 72, p. 305–318, doi:10.1016/S0377-0257(97)90002-1.
Robert, B., Harris, A., Gurioli, L., Médard, E., Sehlke, A., and Whittington, A., 2014, Textural and rheological evolution of basalt flowing down a lava channel: Bulletin of Volcanology, v. 76, p. 1–21, doi:10.1007/s00445-014-0824-8.
Schneider, C.A., Rasband, W.S., and Eliceiri, K.W., 2012, NIH Image to ImageJ: 25 years of image analysis: Nature Methods, v. 9, p. 671–675, doi:10.1038/nmeth.2089.